Augmented Multistep Finite-Control-Set Model Predictive Control for Induction Motor-Drive System

Xinyue Li, Wei Tian, *Member, IEEE*, Qifan Yang, *Graduate Student Member, IEEE*, Petros Karamanakos, *Senior Member, IEEE*, and Ralph Kennel, *Life Fellow, IEEE*

***Abstract*—This article develops an observer-augmented multistep model predictive control strategy with finite-control-set principle to improve the robustness of the control loop against disturbances, including external disturbances, parameter mismatches, and model uncertainties. The influence of the parameter mismatches on the multistep finite-control-set model predictive control is first discussed via simulations and quantified by analyzing the probability of suboptimality. Furthermore, in order to compensate for these effects, the disturbances are included in the system model of the control problem as an extended state and estimated with a disturbance observer. The estimated disturbances as well as the system states are then delivered to the optimization problem of the current control and incorporated for the computation of the solution. The proposed method is then implemented on a dSPACE system and tested under several scenarios. The effectiveness of the proposal is validated with experimental results.**

***Index Terms*—AC drives, disturbance observer (DOB), finite control set, model predictive control (MPC).**

I. Introduction

MODEL predictive control (MPC) was originally implemented for the control of the process industry and has been intensively studied since the 1970 s [1]. Thanks to the development of microprocessors as well as the advances in numerical computation methods, MPC has regained attention in the domain of power electronics with the response requirement of tens to hundreds of microseconds [2]. It serves as a promising method for the control problem and can outperform the conventional control methods in terms of the dynamic response, the straightforward implementation for multivariable systems as well as for the nested cascaded control loops, and the inclusion of constraints [3].

Depending on the control objectives, MPC can be designed as a current controller [4], a torque controller [5], or a speed controller [6]. Because of the advantages of finite-control-set MPC (FCS-MPC), e.g., the simple and straightforward implementation, the ability to handle system constraints, and the simplicity to apply for multiple-input-multiple-output systems [1], it has been deployed for various applications, such as two-level voltage-source inverters [7], three-level neutral point clamped converters [8], cascaded H-bridge inverters [9], and modular multilevel converters [10], [11].

One of the main challenges of FCS-MPC is that solving the underlying optimization problem is time consuming, especially when the prediction horizon is long, i.e., longer than two steps. Thus, the prediction horizon is set to one in most of the previous works on FCS-MPC [7]. The single-step FCS-MPC is conceptually simple and can be normally solved by exhaustively searching all possible solutions. The number of voltage vectors can be reduced by using the deadbeat solution [12] or the direct torque control switching table [13].

Comparing with the numerous works on single-step FCS-MPC, the multistep FCS-MPC has received less attention due to its heavy computational burden. However, it has been shown in, e.g., [8], [14], [15], and [16] that FCS-MPC with a long prediction horizon can improve the control performance, especially for high-order systems, e.g., electrical drives with *LC* filters [14]. As shown, the torque ripple and the total harmonic distortion of the current are significantly reduced with a longer prediction horizon. In [17], the factors that affect the performance of FCS-MPC are identified and discussed. Subsequently, the guidelines for the design of FCS-MPC, e.g., the choice of norm, the tuning of weighting factors, and the length of the sampling interval and of the prediction horizon, are presented and analyzed in detail.

Besides the works focusing on the control algorithms, the efficient implementation of FCS-MPC on real-time control platforms has also been studied. For example, Dorfling et al. [18] implemented a long-horizon FCS-MPC with the sphere decoder on a field-programmable-gate-array (FPGA). However, the sphere decoding algorithm tends to have a higher computational burden at the transient operation. In [19] and [20], the modification of the initialization for the sphere decoding algorithm has been proposed to solve this problem. In [19], different initialization approaches for transient- and steady-state operation of medium-voltage drives were implemented, where the optimization problem is reformulated, in order to obtain a new initial sphere for the sphere decoder during the transient. A similar method was shown in [20]. Moreover, Karamanakos

Manuscript received 20 March 2023; revised 16 June 2023; accepted 5 August 2023. Date of publication 14 August 2023; date of current version 22 September 2023. Recommended for publication by Associate Editor J. Ye. *(Corresponding author: Xinyue Li.)*

Xinyue Li, Wei Tian, Qifan Yang, and Ralph Kennel are with the Institute for Electrical Drive Systems and Power Electronics, Technical University of Munich, 80333 Munich, Germany (e-mail: xinyue.li@tum.de; wei.tian@tum.de; qifan.yang@tum.de; ralph.kennel@tum.de).

Petros Karamanakos is with the Faculty of Information Technology and Communication Sciences, Tampere University, 33101 Tampere, Finland (e-mail: p.karamanakos@ieee.org).

Color versions of one or more figures in this article are available at https://doi.org/10.1109/TPEL.2023.3304950.

Digital Object Identifier 10.1109/TPEL.2023.3304950

et al. [21] reduced the computational complexity of the sphere decoding algorithm during the transient by computing a tighter sphere for the underlying optimization problem.

As it is indicated in [22], the performance of FCS-MPC, being a proportional controller, can be adversely affected by parameter variations. However, such variations during the operation of the power electronic system, e.g., a variable speed drive, are inevitable. For example, the resistance can be affected by the temperature and the inductances are influenced by the ferromagnetic saturation effect of the magnetizing field [23]. In order to tackle this problem, some approaches have been proposed. The min–max MPC computes the minimization problem under the worst case of the control plant, which is considered by computing the maximization problem [24]. The solution of the min–max MPC, however, is relatively conservative and has a high computational cost. Preindl et al. [25] proposed a Lyapunov-based MPC to guarantee the stability of the drive system via an additional Lyapunov-function-based constraint. In [26], an explicit integrator is added to the objective function to reduce the average steady-state error. Moreover, model-free techniques can also be applied to mitigate the problem of parameter mismatches and disturbances, e.g. [27] and [28], to name but a few. Such methods do not require any information on the motor parameters to realize the control. However, they rely on the measurements and require significant time to obtain the necessary information for control purposes.

Another widely applied technique is the implementation of an observer. In [29], a parameter observer of the input inductance and the input resistance was implemented to tackle the adverse effect of model mismatches. Xu et al. [30] applied an online parameter estimator to estimate the rotor resistance to reduce the torque ripple. Nonetheless, the increased number of the target parameters increases the complexity of the online estimator. The disturbance observer (DOB) is a promising method to estimate the disturbances, including the parameter variations as well as the model uncertainty. An additional advantage of such an approach is that the complexity of the observer can also be mitigated [22]. Wallscheid and Ngoumtsa [31] investigated DOBs for the MPC and concluded that the implementation of a DOB can significantly improve the control performance in terms of steady-state error and current harmonics. The authors in [32], [33], and [34] have implemented the DOB to improve the performance of the finite-control-set predictive torque control for induction machines. Xu et al. [35] implemented the DOB for improving the robustness of the deadbeat predictive current control. However, few previous works have investigated the influence of the parameter mismatches and the model uncertainties on the multistep FCS-MPC. Moreover, a systematic design and formulation of the DOB-augmented multistep FCS-MPC has not been discussed yet.

Motivated by the observations mentioned above, a DOB is deployed to identify the errors caused by the parameter mismatches and the model uncertainties. The main contributions of this article can be summarized as follows.

1) This article first investigates the influence of the parameter mismatches on multistep FCS-MPC. To this aim, the influence of parameter mismatches on the unconstrained solution to the multistep FCS-MPC problem is examined. As shown, multistep FCS-MPC has an inherent mechanism to increase its robustness to parameter mismatches, owing to the fact that it directly accounts for the switching nature of the power electronic system. Notwithstanding the foregoing, a probabilistic analysis is presented to show that the parameter mismatches can still deteriorate the performance of the system as they can affect the complete and—to a lesser degree—the applied optimal solution, especially as the length of the prediction horizon increases.
2) To address the observed issues and enhance the robustness of the controller, the system model is augmented with a disturbance term that accounts for the disturbances, including external disturbances, parameter mismatches, and model uncertainties. Subsequently, a Kalman filter (KF) is designed to estimate the aforementioned disturbance.
3) The estimated state is used in the underlying optimization problem to enhance the robustness of multistep FCS-MPC. As demonstrated with the presented experimental results with an induction motor-drive system, the proposed scheme provides high robustness to parameter variations, model inaccuracies, etc., thus achieving superior steady-state and transient performance.

The rest of this article is organized as follows. In Section II, the model of the induction motor and the principle of multistep FCS-MPC are introduced. In Section III, the effects of the parameter mismatch on multistep FCS-MPC are analyzed with simulations. The probability of obtaining a suboptimal solution for the multistep FCS-MPC problem under the existence of parameter mismatches is also presented. Moreover, the augmented system and the general formulation of the optimization problem for direct current control of IM are given. In Section IV, the proposed method is verified with experimental results and compared with the conventional multistep FCS-MPC under the parameter mismatches. Moreover, the transient performance of the discussed methods is further compared, including a load-step test and a speed-step test. Finally, Section V concludes this article.

II. Problem Statement

A. Induction Motor

The state variables for the current control of a squirrel-cage induction machine are chosen as the stator current $\boldsymbol{i}_s$ and the rotor flux $\boldsymbol{\psi}_r$. The corresponding state-space formulation of an induction machine (IM) in the $\alpha\beta$ reference frame is given in the continuous-time domain as

$$\dot{\boldsymbol{x}} = \boldsymbol{A}_c\,\boldsymbol{x} + \boldsymbol{B}_c\,\boldsymbol{v}_s \tag{1}$$

with $\boldsymbol{x} = \begin{bmatrix} \boldsymbol{i}_s^T & \boldsymbol{\psi}_r^T \end{bmatrix}^T$ and

$$\boldsymbol{A}_c = \begin{bmatrix} -\frac{L_r^2 R_s + L_m^2 R_r}{L_r \sigma} & 0 & \frac{L_m L_r}{L_r \sigma} & \frac{L_m}{\sigma}\omega_r \\ 0 & -\frac{L_r^2 R_s + L_m^2 R_r}{L_r \sigma} & -\frac{L_m}{\sigma}\omega_r & \frac{L_m L_r}{L_r \sigma} \\ R_r \frac{L_m}{L_r} & 0 & -\frac{R_r}{L_r} & -\omega_r \\ 0 & R_r \frac{L_m}{L_r} & \omega_r & -\frac{R_r}{L_r} \end{bmatrix}$$

$$\boldsymbol{B}_c = \begin{bmatrix} \frac{L_r}{\sigma} & 0 \\ 0 & \frac{L_r}{\sigma} \\ 0 & 0 \\ 0 & 0 \end{bmatrix} \tag{2}$$

where $\sigma = L_r L_s - L_m^2$. L_r, L_s, and L_m denote the rotor inductance, the stator inductance, and the mutual inductance, respectively. R_s represents the stator resistance. R_r is the rotor resistance. ω_r denotes the angular speed of the rotor.

B. Multistep FCS-MPC

Multistep FCS-MPC relies on the system model and solves an optimization problem for the reference tracking based on the predictions of the system state. The system (1) can be discretized with the forward Euler method or the exact discretization, and is rewritten for the purpose of compactness as

$$\begin{aligned} \boldsymbol{x}(k+1) &= \boldsymbol{A}_d\, \boldsymbol{x}(k) + \boldsymbol{B}_d\, \boldsymbol{v}_s(k) \\ \boldsymbol{y}(k) &= \boldsymbol{C}_d\, \boldsymbol{x}(k). \end{aligned} \tag{3}$$

The principle of the multistep FCS-MPC for the current control of the IM at the time step k is to solve an optimization problem Ω, which can be written without the loss of generality as follows [36]:

$$\begin{aligned} \underset{\mathbf{U}(k)}{\text{minimize}} \quad & J \\ \text{subject to} \quad & \boldsymbol{x}(j+1) = \boldsymbol{A}_d\, \boldsymbol{x}(j) + \boldsymbol{B}_d\, \boldsymbol{T}_c\, \boldsymbol{u}(j) \\ & \boldsymbol{u}(j) \in \mathbb{U} \times \mathbb{U} \times \mathbb{U} \end{aligned} \tag{4}$$

where $j = k, k+1, \ldots, k+N_p-1$. $\boldsymbol{T}_c$ represents the simplified Clarke transformation, which transforms the quantities from the three-phase system into the two-phase system. $\boldsymbol{u}$ denotes the three-phase switch position of the system, i.e., $\boldsymbol{u} = [u_a \quad u_b \quad u_c]^T$. $\boldsymbol{y}_r$ is the reference current and $\mathbf{U}$ denotes the sequence of solutions for the optimization problem in (4). It can be written as $\mathbf{U}(k) := [\boldsymbol{u}(k)^T \quad \boldsymbol{u}(k+1)^T \ldots \boldsymbol{u}(k+N_p-1)^T]^T$. The cost function J of (4) is designed such that a tradeoff between the accuracy of reference tracking and the switching effort is created. It can be formulated as

$$\begin{aligned} J = & \sum_{j=k}^{k+N_p-1} \|\boldsymbol{y}_r(j+1) - \boldsymbol{C}_d\, \boldsymbol{x}(j+1)\|_2^2 \\ & + \lambda \|\boldsymbol{u}(j) - \boldsymbol{u}(j-1)\|_2^2 \end{aligned} \tag{5}$$

where λ is the weighting factor to proceed the tradeoff. For multistep FCS-MPC problem, the control input constraint $\mathbb{U}$ denotes the possible switching actions of the three phases and is given in the following for the two-level inverters:

$$\mathbb{U} := \{0, 1\}. \tag{6}$$

Each value in $\mathbb{U}$ represents the output voltage of the inverter as 0 and U_{dc}, respectively.

The optimization problem Ω in (4) is a mixed-integer quadratic programming problem. The most straightforward way to solve it is via an exhaustive search, which enumerates all possible switching combinations and evaluates the cost function accordingly. It is efficient and suitable for a short prediction horizon. However, the computational complexity of the exhaustive search grows exponentially in the worst case with the prediction horizon N_p. In order to tackle this problem, several works have been carried out [15], [36]. In this article, the modified sphere decoding algorithm from [36] is implemented, where the solution of (4) is obtained with

$$\mathbf{U}^* = \arg \min_{\mathbf{U}(k)} \|\mathbf{H}\mathbf{U}(k) - \mathbf{U}_{\text{unc}}(k)\|_2^2 \tag{7}$$

where $\mathbf{H}$ is the generator matrix, which forms the search space for Ω. Its computation is then shown in the following section. $\mathbf{U}_{\text{unc}}(k) = \mathbf{H}\mathbf{U}^o_{\text{unc}}(k)$, where $\mathbf{U}^o_{\text{unc}}(k)$ is the solution of (4) omitting the constraint $\mathbb{U}$.

III. Proposed Observer-Augmented Multistep FCS-MPC Strategy

The discrete nature of multistep FCS-MPC can alleviate the effects of the disturbances to a certain level. The disturbances, incorporating the parameter variations, the external disturbances, and the unmodeled uncertainties, do not necessarily affect the solution of the optimization problem of multistep FCS-MPC. Nonetheless, the unconstrained solution $\mathbf{U}_{\text{unc}}$ will be heavily influenced by the disturbances, which may lead to a suboptimal solution for the problem (4). However, the discrete nature of FCS-MPC impedes the analysis as well as the quantification of these effects. Hence, these are discussed in this section with the help of simulations.

A. Influence of the Parameter Mismatch on Multistep FCS-MPC

Several simulations were carried out to indicate the effects of the parameter mismatches on the solution of the optimization problem (4) and the control performance of the multistep FCS-MPC for IM. The multistep FCS-MPC is designed such that the switching frequency is in the range of a few kHz. The solutions to the optimization problem in (4) with and without the parameter mismatch of L_m are compared and shown in Fig. 1.

In order to differentiate the optimization problem for the nominal system and the system with parameter mismatch of L_m, $\bar{\Omega}$ and Ω are deployed to represent them, respectively. The unconstrained solutions $\bar{\mathbf{U}}_{\text{unc}}$ and $\mathbf{U}_{\text{unc}}$ have a slight difference, which can be observed in Fig. 1. The sphere determined by $\bar{\mathbf{U}}_{\text{unc}}$ as the circle center and $\bar{\mathbf{U}}^*$ is larger than that of the optimization problem Ω, which is not necessarily true for all working points of IM. In spite of the small difference between the unconstrained solutions $\bar{\mathbf{U}}_{\text{unc}}$ and $\mathbf{U}_{\text{unc}}$, different final solutions, i.e., $\mathbf{U}^*$ and $\bar{\mathbf{U}}^*$, are found for $\bar{\Omega}$ and Ω.

B. Probability of Suboptimal Solution Under the Parameter Mismatch

The integer characteristic of FCS-MPC impedes the quantification of the effects of the disturbances. Simulations on the admissible region of i_α and i_β regarding different parameter variations have been conducted in order to study the incidence of the varied solutions. The prediction horizon N_p is an important

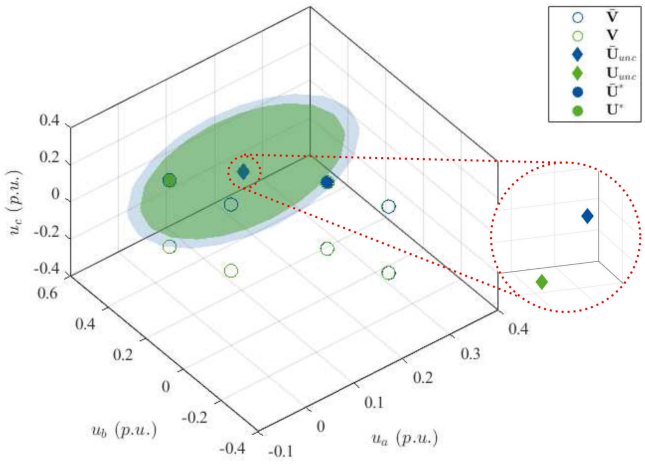

Fig. 1. Comparison of solutions of (4) between the scenarios with and without the L_m mismatch. The empty circles denote all the switching candidates $\boldsymbol{V}$. The filled diamonds represent the unconstrained solution $\mathbf{U}_{\text{unc}}$ and the filled circles depict the solution $\mathbf{U}^*$. The superscript $\bar{\cdot}$ denotes the quantities in the nominal system without the parameter mismatch, which is shown in blue. The quantities in the disturbed system are presented in green.

parameter for multistep FCS-MPC. Therefore, the probabilities of suboptimal solutions with different prediction horizons varying from $N_p = 1$ to $N_p = 10$ have been evaluated. The simulations were conducted in various operating points ranging from the no-load condition to the full-load condition with a step of 10% of the rated torque.

The results of obtaining a suboptimal $\mathbf{U}(k)$ and a suboptimal $\boldsymbol{u}(k)$ are summarized in Fig. 2 and Fig. 3, respectively. Since a similar phenomenon can be observed between $L_{\sigma r}$ (rotor leakage inductance) and $L_{\sigma s}$ (stator leakage inductance) as well as between R_r and R_s, the simulation results of $L_{\sigma r}$, R_r, and L_m are selected and presented. The probabilities, as shown in Figs. 2 and 3, are defined as the ratio between the number of incidents with the suboptimal solutions (different from the solutions in the nominal condition) and the number of all simulations. The simulation results of $r_p = 50\%$ and $r_p = 200\%$ are also analogous, where r_p is the ratio for adapting the parameter of interest in the controller and is defined by

$$r_p = \frac{p_c}{p_m} \times 100\% \tag{8}$$

where p_c is the parameter utilized in the controller and p_m is the nominal parameter of the IM.

As it is shown in Fig. 2, the probability $\mathcal{P}$ of obtaining the suboptimal $\mathbf{U}(k)$ increases with the prediction horizon N_p, which can be explained by the fact that the existing model errors accumulate as the prediction horizon N_p grows.

The probability of applying a suboptimal solution $\boldsymbol{u}(k)$ to the inverter is also studied since only the first element of $\mathbf{U}(k)$ is applied for the control. The results are shown in Fig. 3. It is worth mentioning that a relative lower probability of suboptimality can be observed in the cases where the prediction horizon is selected as 1, 2, and 5. In all parameter variation scenarios, $N_p = 3$ has the highest probability to select the suboptimal solution.

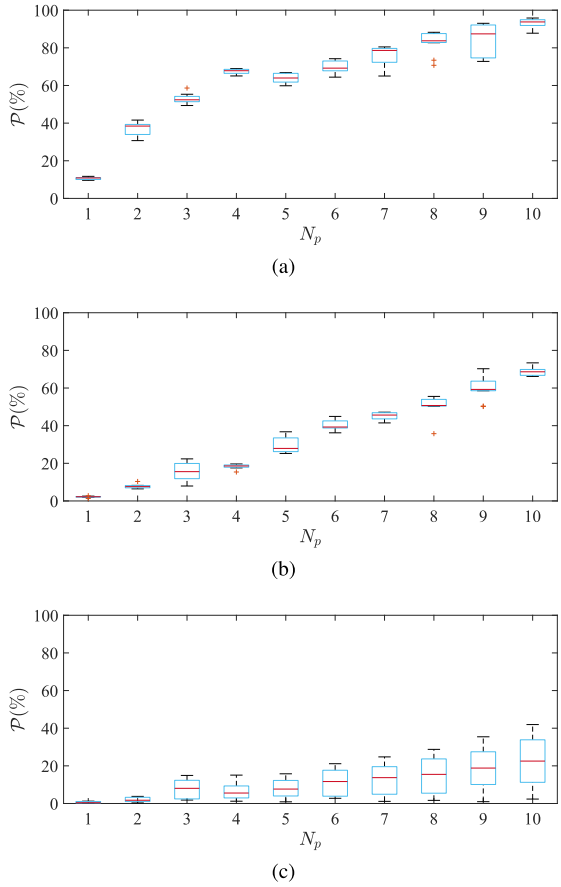

Fig. 2. Probability of choosing different $\mathbf{U}(k)$ to the nominal condition considering different N_p and various parameter variations. (a) Denotes the influence of $L_{\sigma r}$ with $r_{L_{\sigma r}} = 50\%$. (b) Represents the effects from L_m with a ratio of 50%. (c) Shows the influence of R_r, where $r_{R_r} = 50\%$.

C. Augmented System Model

In order to tackle the problem caused by the disturbances, such as external disturbances, model uncertainties, and parameter mismatches, a DOB is deployed to estimate the disturbance $\boldsymbol{\epsilon}$. The augmented model of an IM for the DOB can be written as

$$\begin{bmatrix} \boldsymbol{x}(k+1) \\ \boldsymbol{\epsilon}(k+1) \end{bmatrix} = \underbrace{\begin{bmatrix} \boldsymbol{A}_d & (\boldsymbol{I}\,\mathbf{0})^T \\ \mathbf{0} & \boldsymbol{I} \end{bmatrix}}_{:=\boldsymbol{A}_d^a} \begin{bmatrix} \boldsymbol{x}(k) \\ \boldsymbol{\epsilon}(k) \end{bmatrix} + \underbrace{\begin{bmatrix} \boldsymbol{B}_d \\ \mathbf{0} \end{bmatrix}}_{:=\boldsymbol{B}_d^a} \boldsymbol{v}_s(k)$$

$$\boldsymbol{y}(k) = \underbrace{\begin{bmatrix} \boldsymbol{C}_d & \mathbf{0} \end{bmatrix}}_{:=\boldsymbol{C}_d^a} \begin{bmatrix} \boldsymbol{x}(k) \\ \boldsymbol{\epsilon}(k) \end{bmatrix} \tag{9}$$

where $\boldsymbol{x} \in \mathbb{R}^{4\times1}$, $\boldsymbol{\epsilon} \in \mathbb{R}^{2\times1}$, $\boldsymbol{A}_d^a \in \mathbb{R}^{6\times6}$, $\boldsymbol{B}_d^a \in \mathbb{R}^{6\times2}$, and $\boldsymbol{C}_d^a \in \mathbb{R}^{2\times6}$. As it is concluded in [37], a KF can obtain relatively accurate estimation results and has a tolerable computational burden for estimating slowly varying parameters. Therefore, a KF is employed for estimating the disturbances $\boldsymbol{\epsilon}$. A KF consists of two steps. The first step is the prediction, which predicts the system propagation based on the system dynamics. The second step is the update, which corrects the prediction with the most

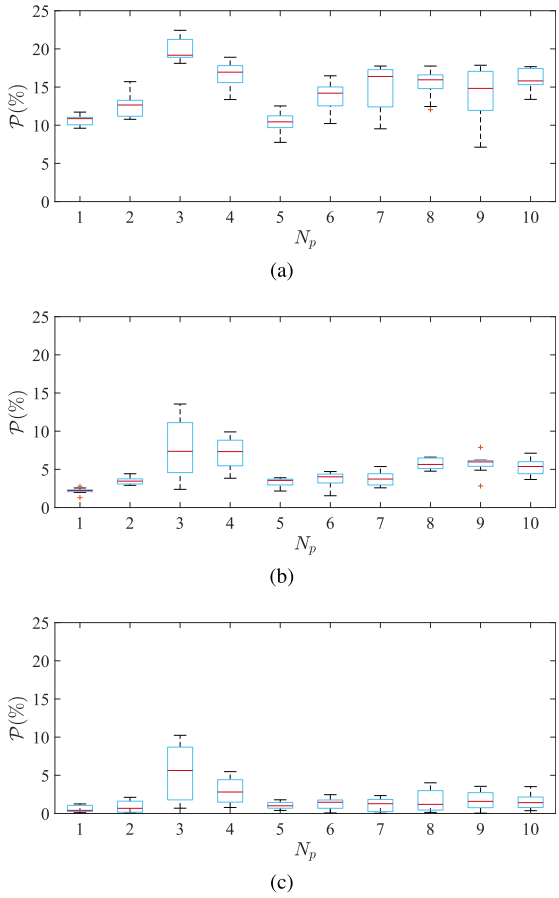

Fig. 3. Probability distribution of choosing different $\boldsymbol{u}(k)$ to nominal condition for different N_p and various parameter mismatches. (a)–(c) Denote the influence of $L_{\sigma r}$, L_m, and R_r with a ratio of 50%, respectively.

recent measurement. The computation procedure of KF for the system (9) at the time step k can be written as

Prediction:

$$\hat{\boldsymbol{x}}_{k|k-1} = \boldsymbol{A}^a_{d,k-1}\hat{\boldsymbol{x}}_{k-1|k-1} + \boldsymbol{B}^a_d\boldsymbol{u}_{k-1} \tag{10}$$
$$\boldsymbol{P}_{k|k-1} = \boldsymbol{A}^a_{d,k-1}\boldsymbol{P}_{k-1|k-1}{\boldsymbol{A}^a_{d,\,k-1}}^T + \boldsymbol{Q}$$

Update:

$$\begin{aligned}\tilde{\boldsymbol{y}}_n &= \boldsymbol{y}_n - \boldsymbol{C}^a_d\,\hat{\boldsymbol{x}}_{k|k-1}\\ \boldsymbol{S}_n &= \boldsymbol{C}^a_d\boldsymbol{P}_{k|k-1}\boldsymbol{C}^{aT}_d + \boldsymbol{R}\\ \boldsymbol{K}_n &= \boldsymbol{P}_{k|k-1}\boldsymbol{C}^{aT}_d\boldsymbol{S}^{-1}_n\\ \hat{\boldsymbol{x}}_{k|k} &= \hat{\boldsymbol{x}}_{k|k-1} + \boldsymbol{K}_n\tilde{\boldsymbol{y}}_n\\ \boldsymbol{P}_{k|k} &= (\boldsymbol{I} - \boldsymbol{K}_n\boldsymbol{C}^a_d)\boldsymbol{P}_{k|k-1}\end{aligned} \tag{11}$$

where $\boldsymbol{Q}$ and $\boldsymbol{R}$ denote the covariance matrices of the system and measurement noise, respectively.

D. Multistep FCS-MPC With Increased Robustness

The complete block diagram of the proposed observer-augmented multistep FCS-MPC control strategy is shown in Fig. 4. As can be seen, the proposed multistep FCS-MPC algorithm consists of the KF-based DOB and the multistep FCS-MPC algorithm that accounts for the disturbances. First, the three-phase current is measured at time step k and transformed into the $\alpha\beta$ reference frame. With $\boldsymbol{i}(k)$, the previously applied switch position $\boldsymbol{u}(k-1)$ and the measured motor speed, the estimated values, i.e., $\hat{\boldsymbol{i}}_s$, $\hat{\boldsymbol{\psi}}_r$, and $\hat{\boldsymbol{\epsilon}}$ are computed based on the steps described in (10) and (11). Subsequently, the estimated system states $\hat{\boldsymbol{i}}_s$, $\hat{\boldsymbol{\psi}}_r$, and $\hat{\boldsymbol{\epsilon}}$ are delivered to the multistep FCS-MPC scheme in order to compute the optimal three-phase switch position at step k, i.e., $\boldsymbol{u}^*(k)$. To do so, problem (4) needs to be reformulated. Specifically, with the help of (9), problem (4) becomes

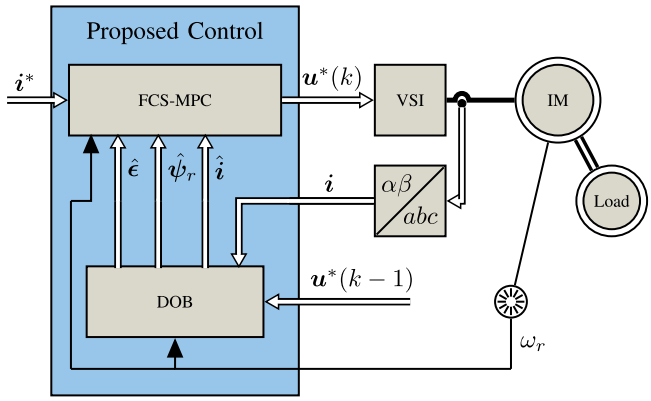

Fig. 4. Proposed augmented FCS-MPC control strategy for the induction motor-drive systems.

$$\begin{aligned}\underset{\mathbf{U}(k)}{\text{minimize}}\quad & J\\ \text{subject to}\quad & \hat{\boldsymbol{x}}(j+1) = \boldsymbol{A}_d\,\hat{\boldsymbol{x}}(j) + \boldsymbol{B}_d\,\boldsymbol{T}_c\,\boldsymbol{u}(j) + (\boldsymbol{I}\;\boldsymbol{0})^T\hat{\boldsymbol{\epsilon}}(j)\\ & \boldsymbol{u}(j) \in \mathbb{U}\times\mathbb{U}\times\mathbb{U}\end{aligned} \tag{12}$$

where

$$\begin{aligned}J = \sum_{j=k}^{k+N_p-1} & \|\boldsymbol{y}_r(j+1) - \boldsymbol{C}_d\,\hat{\boldsymbol{x}}(j+1)\|_2^2\\ & + \lambda\|\boldsymbol{u}(j) - \boldsymbol{u}(j-1)\|_2^2.\end{aligned} \tag{13}$$

The cost function can be reformulated in a compact form as

$$J = \theta(k) + 2(\boldsymbol{\Theta}(k))^T\mathbf{U}(k) + \|\mathbf{U}(k)\|^2_{\boldsymbol{M}} \tag{14}$$

where

$$\begin{aligned}\theta(k) &:= \|\boldsymbol{Y}_r - \boldsymbol{\Gamma}\,\hat{\boldsymbol{x}}(k) - \boldsymbol{\Xi}\,\hat{\boldsymbol{\epsilon}}(k)\|_2^2 + \lambda\|\boldsymbol{E}\,\boldsymbol{u}(k-1)\|_2^2\\ \boldsymbol{\Theta}(k) &:= ((\boldsymbol{Y}_r - \boldsymbol{\Gamma}\,\hat{\boldsymbol{x}}(k) - \boldsymbol{\Xi}\,\hat{\boldsymbol{\epsilon}}(k))^T\,\boldsymbol{\Upsilon} - \lambda(\boldsymbol{E}\boldsymbol{u}(k-1))^T\boldsymbol{S})^T\\ \boldsymbol{M} &:= \boldsymbol{\Upsilon}^T\boldsymbol{\Upsilon} + \lambda\,\boldsymbol{S}^T\boldsymbol{S}\end{aligned}$$

where $\boldsymbol{M} = \mathbf{H}^T\mathbf{H}$. $\boldsymbol{Y}_r := [\boldsymbol{y}_r(k)^T \;\; \boldsymbol{y}_r(k+1)^T \;\ldots\; \boldsymbol{y}_r(k+N_p-1)^T]^T$ denotes the N_p replicates of $\boldsymbol{y}_r$ and $\boldsymbol{Y}_r \in \mathbb{R}^{2N_p\times 1}$. The matrices $\boldsymbol{\Gamma} \in \mathbb{R}^{2N_p\times 4}$, $\boldsymbol{\Xi} \in \mathbb{R}^{2N_p\times 2}$, $\boldsymbol{\Upsilon} \in \mathbb{R}^{2N_p\times 3N_p}$,

Procedure 1: Multistep FCS-MPC With Increased Robustness.

1: Measure the current and speed.
2: Compute the estimates based on the aforementioned measurements, via (10) and (11).
3: Include the estimation results for the optimization problem in (15).
4: Solve the optimization problem in (15) with the sphere decoder.
5: Obtain the optimal sequence $\mathbf{U}^*(k)$.
6: Apply the optimal three-phase switch position $\boldsymbol{u}^*(k)$.

$\boldsymbol{S} \in \mathbb{R}^{3N_p \times 3N_p}$, and $\boldsymbol{E} \in \mathbb{R}^{3N_p \times 3}$ are given in the following:

$$\boldsymbol{\Gamma} = \begin{bmatrix} \boldsymbol{C}_d\boldsymbol{A}_d \\ \boldsymbol{C}_d\boldsymbol{A}_d{}^2 \\ \vdots \\ \boldsymbol{C}_d\boldsymbol{A}_d{}^{N_p} \end{bmatrix}, \quad \boldsymbol{S} = \begin{bmatrix} \boldsymbol{I} & \boldsymbol{0} & \dots & \boldsymbol{0} \\ -\boldsymbol{I} & \boldsymbol{I} & \dots & \boldsymbol{0} \\ \boldsymbol{0} & -\boldsymbol{I} & \dots & \boldsymbol{0} \\ \vdots & \vdots & \ddots & \vdots \\ \boldsymbol{0} & \boldsymbol{0} & \dots & \boldsymbol{I} \end{bmatrix}, \quad \boldsymbol{E} = \begin{bmatrix} \boldsymbol{I} \\ \boldsymbol{0} \\ \boldsymbol{0} \\ \vdots \\ \boldsymbol{0} \end{bmatrix}$$

$$\boldsymbol{\Upsilon} = \begin{bmatrix} \boldsymbol{C}_d\boldsymbol{B}_d\boldsymbol{T}_c & \boldsymbol{0} & \dots & \boldsymbol{0} \\ \boldsymbol{C}_d\boldsymbol{A}_d\boldsymbol{B}_d\boldsymbol{T}_c & \boldsymbol{C}_d\boldsymbol{B}_d\boldsymbol{T}_c & \dots & \boldsymbol{0} \\ \vdots & \vdots & \ddots & \vdots \\ \boldsymbol{C}_d\boldsymbol{A}_d{}^{N_p-1}\boldsymbol{B}_d\boldsymbol{T}_c & \boldsymbol{C}_d\boldsymbol{A}_d{}^{N_p-2}\boldsymbol{B}_d\boldsymbol{T}_c & \dots & \boldsymbol{C}_d\boldsymbol{B}_d\boldsymbol{T}_c \end{bmatrix}$$

$$\boldsymbol{\Xi} = \begin{bmatrix} \boldsymbol{C}_d(\boldsymbol{I}\,\boldsymbol{0})^T \\ (\boldsymbol{C}_d\boldsymbol{A}_d + \boldsymbol{C}_d)(\boldsymbol{I}\,\boldsymbol{0})^T \\ \vdots \\ (\boldsymbol{C}_d\boldsymbol{A}_d{}^{N_p-1} + \boldsymbol{C}_d\boldsymbol{A}_d{}^{N_p-2} + \cdots + \boldsymbol{C}_d)(\boldsymbol{I}\,\boldsymbol{0})^T \end{bmatrix}.$$

As a result, the optimization problem for the proposed control strategy can be compactly written as an integer least-squares problem of the form

$$\begin{aligned} \mathbf{U}^*(k) = \arg \quad & \underset{\mathbf{U}(k)}{\text{minimize}} \|\mathbf{H}\mathbf{U}(k) - \mathbf{U}_{\text{unc}}(k)\|_2^2 \\ \text{subject to} \quad & \boldsymbol{u}(j) \in \mathbb{U} \times \mathbb{U} \times \mathbb{U} \\ & j = k, \dots, k + N_p - 1 \end{aligned} \tag{15}$$

where $\mathbf{U}_{\text{unc}}(k) = -\mathbf{H}\boldsymbol{M}^{-1}\boldsymbol{\Theta}(k)$. Subsequently, problem (15) can be solved with the sphere decoding algorithm [36]. The complete procedure of the proposed method is given in Procedure 1.

E. Stability Analysis

The closed-loop stability of power electronic systems controlled with multistep FCS-MPC has been discussed in works, such as [38] and [39]. However, the stability analysis is limited to systems that do not account for external disturbances, model uncertainties, etc. Therefore, in the following, the stability analysis for the system controlled with the proposed approach is given.

By assuming $N_p = 1$, the cost function in (12) can be written as[1]

$$\begin{aligned} J = \|\Delta\boldsymbol{y}(k+1) - \kappa\,\boldsymbol{T}_c\,\Delta\boldsymbol{u}(k) \\ + \boldsymbol{e}(k) - \hat{\boldsymbol{\epsilon}}(k)\|_2^2 + \lambda\|\Delta\boldsymbol{u}(k)\|_2^2 \end{aligned} \tag{16}$$

where

$$\begin{aligned} \Delta\boldsymbol{y}(k+1) &= \boldsymbol{y}_r(k+1) - \boldsymbol{C}_d\,\boldsymbol{A}_d\,\boldsymbol{x}(k) \\ &\quad - \boldsymbol{C}_d\,\boldsymbol{B}_d\,\boldsymbol{T}_c\,\boldsymbol{u}(k-1) \\ \boldsymbol{e} &= \boldsymbol{C}_d\,\boldsymbol{A}_d\,(\boldsymbol{x}(k) - \hat{\boldsymbol{x}}(k)) \end{aligned} \tag{17}$$

and κ denotes the diagonal elements of $\boldsymbol{C}_d\,\boldsymbol{B}_d$ since the matrix $(\boldsymbol{C}_d\,\boldsymbol{B}_d) \in \mathbb{R}^{2\times 2}$ is approximately diagonal [39]. By applying the analysis given in [39], the cost function can be written as[2]

$$\begin{aligned} J = \quad & \kappa^2\,\Delta\boldsymbol{u}^T\,\boldsymbol{T}_c^T\,\boldsymbol{T}_c\,\Delta\boldsymbol{u} - 2\,\kappa\,(\Delta\boldsymbol{y} + \boldsymbol{e} - \hat{\boldsymbol{\epsilon}})^T\,\boldsymbol{T}_c\,\Delta\boldsymbol{u} \\ & + \lambda\,\Delta\boldsymbol{u}^T\,\Delta\boldsymbol{u} + \|\Delta\boldsymbol{y} + \boldsymbol{e} - \hat{\boldsymbol{\epsilon}}\|_2^2 \\ = \quad & \|\Delta\boldsymbol{u} + \boldsymbol{M}^{-1}\boldsymbol{N}\|_{\boldsymbol{M}}^2 + c \end{aligned} \tag{18}$$

where

$$\begin{aligned} \boldsymbol{M} &= \kappa^2\,\Delta\boldsymbol{T}_c^T\,\boldsymbol{T}_c + \lambda\,\boldsymbol{I} \\ \boldsymbol{N} &= -\left[\,\kappa\,(\Delta\boldsymbol{y} + \boldsymbol{e} - \hat{\boldsymbol{\epsilon}})^T\,\boldsymbol{T}_c\right]^T \\ c &= \|\Delta\boldsymbol{y} + \boldsymbol{e} - \hat{\boldsymbol{\epsilon}}\|_2^2 - \boldsymbol{N}^T\boldsymbol{M}^{-1}\boldsymbol{N}. \end{aligned} \tag{19}$$

As shown in [40], the estimation error $\boldsymbol{e}$ with KF is exponentially bounded and the estimates converge in a mean-square manner. Based on the above, and since problem (12) is a quadratic program with the integer optimization variable $\mathbf{U}$, it can be concluded that the practical stability of the system is guaranteed, as shown in [39].

IV. Experimental Evaluation

The proposed method is validated with experiments. The experimental setup of the drive system is shown in Fig. 5. The proposed control strategy and the conventional multistep FCS-MPC are implemented on a dSPACE SCALEXIO real-time system in order to evaluate their performance under the existence of parameter mismatches and test the performance of the proposed strategy during transient. The block diagram of the experimental setup is shown in Fig. 6. The dSPACE SCALEXIO unit consists of one processor unit (Intel XEON E3V6 CPU, 3.8 GHz, 4 cores), one FPGA board (Xilinx Kintex-7 160 T), one analog-to-digital conversion (ADC) board (DS6221), and one digital IO board (DS2655M2). All the algorithms are implemented in the CPU. The CPU minimum processing time (including communication and ADC conversion time) is $8\,\mu$s. The sampling frequency is set to $f_s = 10\,$kHz. The gating signals are generated by the dSPACE DS2655 FPGA board, which has a device timing of $125\,$MHz. The gating signals are sent from

[1] Note that the extension of the following analysis to longer horizons, although laborious, is straightforward.

[2] Note that, in the following expressions, the time indication has been dropped to simplify the notation.

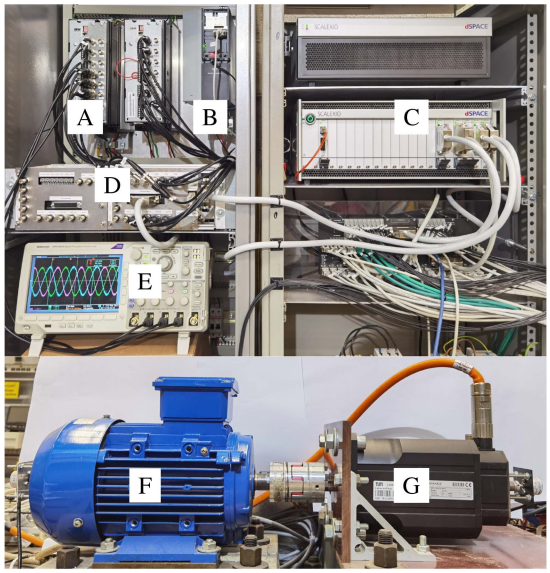

Fig. 5. Setup of the electrical drives test bench. A: SEW inverter for IM, B: Danfoss inverter for load PMSM, C: dSPACE SCALEXIO real-time control system, D: Interface, E: Oscilloscope, F: IM, G: PMSM.

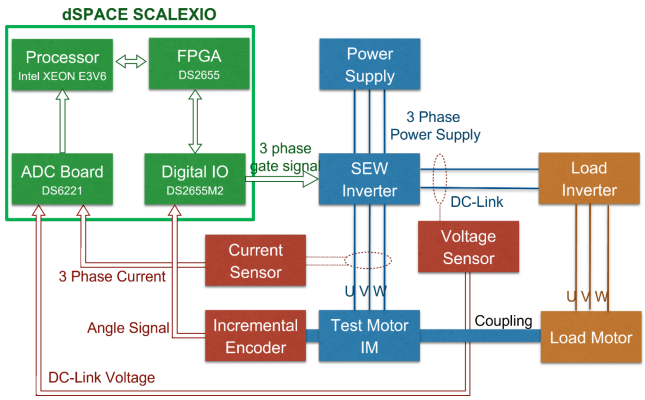

Fig. 6. Block diagram of the experimental setup.

the dSPACE to a three-phase two-level SEW MDX inverter. The ADC is performed by the dSPACE DS6221 A/D board, which has a minimum conversion time of 250 ns. The dc-link voltage is fixed to a value of around 560 V. The rotor position is acquired with a 1024-ppr incremental encoder. The parameters of the investigated induction motor are given in Table I. The IM is coupled with a permanent magnet synchronous motor rated 2 kW, 6 Nm. The KF is employed to estimate the disturbance and the current, of which the measurement noise covariance matrix was selected as the identity matrix and the process noise covariance matrix was set as a diagonal matrix such that the elements are around 10% of the individual state value. More comments on the design of the estimators can be found in [41]. The outer control loop, i.e., the speed loop, is designed based on a proportional–integral controller and was configured with the control parameters computed from the symmetric optimum, resulting in the proportional gain $k_p = 2.2359$ and the integration gain $k_i = 0.1133$.

TABLE I
PARAMETERS OF THE IM

Parameter	Symbol	Value
Rated current	I_N	4.61 A
Rated speed	w_{mN}	2840 r/min
Rated power	P_N	2.2 kW
Rated torque	T_N	7.4 Nm
Number of pole pairs	n_p	1
Nominal stator resistance	R_s	2.8225 Ω
Nominal rotor resistance	R_r	2.2684 Ω
Nominal stator inductance	L_s	243.6 mH
Nominal rotor inductance	L_r	243.6 mH
Nominal mutual inductance	L_m	233.8 mH

A. Performance Under Parameter Mismatches for $N_p = 1$

The proposed control strategy is compared with the conventional multistep FCS-MPC in the existence of parameter mismatches. First, their performances with $N_p = 1$ are compared. The average switching frequency f_sw shown in this section is computed with

$$f_\mathrm{sw} = \frac{1}{m\,M\,T_s}\sum_{j=1}^{M}\|\boldsymbol{u}(j) - \boldsymbol{u}(j-1)\|_1 \tag{20}$$

where m is the number of switches and M is the length of the averaged window. The IM runs at 50% of the rated speed. The proposed control strategy was activated at $t = 2\,\mathrm{s}$. The corresponding experimental results, including measurements on the currents and the switching frequency f_sw, are shown in Fig. 7.

As it is shown in Fig. 7, an obvious steady-state error can be observed before $t = 2\,\mathrm{s}$ in all scenarios, especially at $r_{L_m} = 150\%$, as shown in Fig. 7(g) and (h), where large ripples and control bias can be observed. After the activation of the proposed control strategy, the steady-state error is considerably alleviated. At the nominal condition and $r_{L_m} = 67\%$, the proposed control strategy reaches the new steady state immediately after the activation. At $r_{L_m} = 150\%$, the transient after the activation lasts longer. Moreover, the switching frequency has significantly reduced in all test cases after switching to the proposed method.

B. Performance Under Parameter Mismatches for $N_p = 5$

The proposed control strategy is further tested for $N_p = 5$ and compared with the conventional multistep FCS-MPC. The experimental results are shown in Fig. 8. It is worth mentioning that larger ripples than the results under the control with $N_p = 1$ can be observed, which may result from the lower switching frequencies. After activating the proposed method, the bias that can be noticed under the control of the conventional multistep FCS-MPC is effectively mitigated. Moreover, smaller current ripples can be observed at $r_{L_m} = 100\%$ and $r_{L_m} = 150\%$ with the proposed controller, even though the switching frequencies are lower. Similar to the conclusions drawn for the case, where $N_p = 1$, the transient of the activation lasts only a short time and the system reaches the new steady state promptly. Moreover, the estimated disturbances under $r_{L_m} = 67\%$ and $r_{L_m} = 150\%$

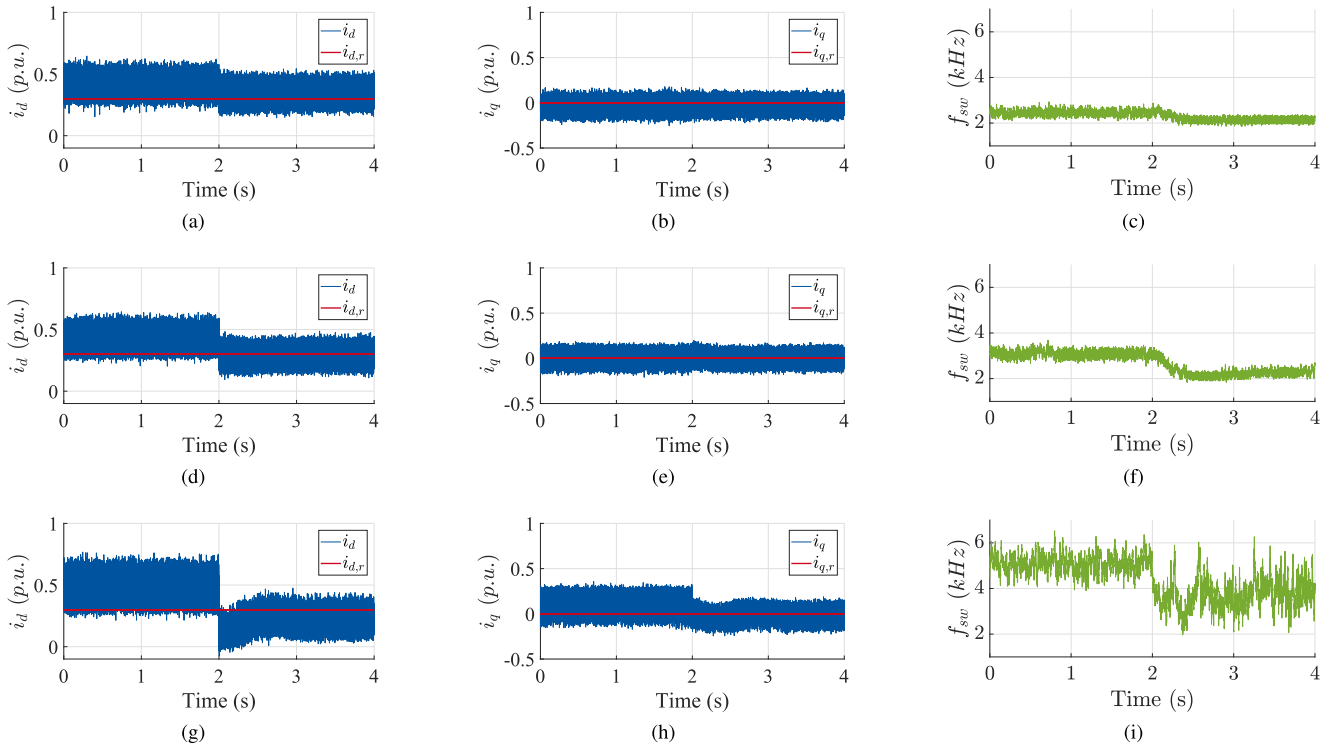

Fig. 7. Comparison of the conventional FCS-MPC and the proposed control strategy with $N_p = 1$ under the parameter variation of L_m. The proposed control strategy is activated at $t = 2$ s. (a)–(c) Show the experimental results under $r_{L_m} = 67\%$. (d)–(f) Denote the performance of the controllers in nominal condition. (g)–(i) Represent the results with $r_{L_m} = 150\%$.

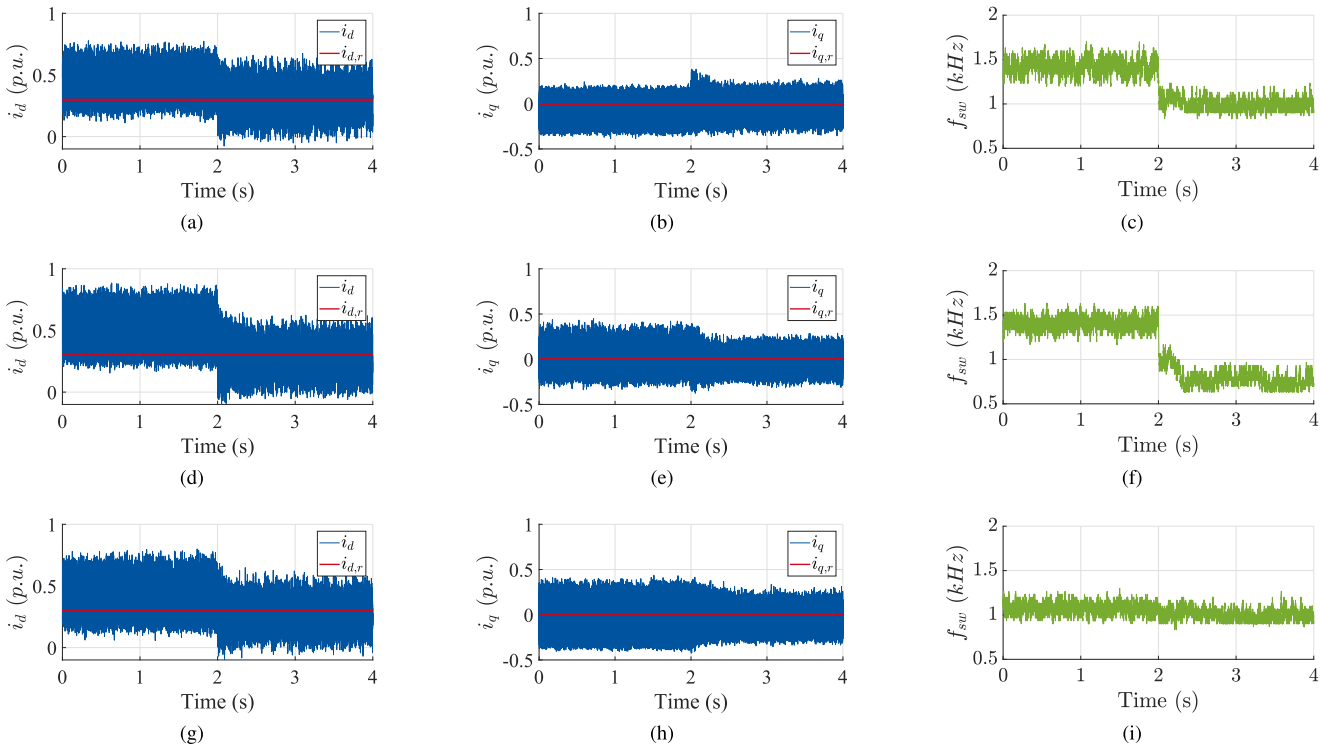

Fig. 8. Comparison of the conventional FCS-MPC and the proposed control strategy with $N_p = 5$ under the parameter variation of L_m. The proposed control strategy is activated at $t = 2$ s. (a)–(c) Show the experimental results under $r_{L_m} = 67\%$. (d)–(f) Denote the performance of the controllers in nominal situation. (g)–(i) Represent the results with under $r_{L_m} = 150\%$.

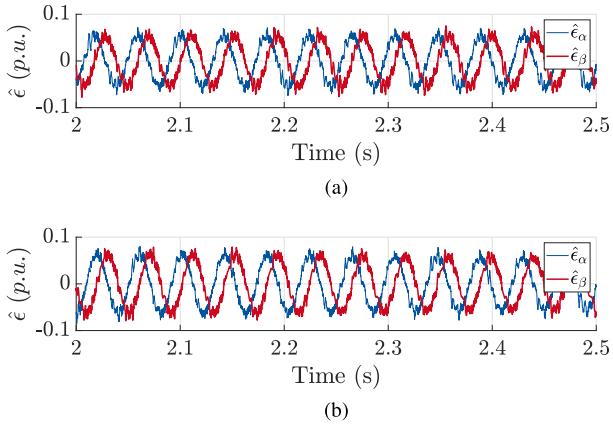

Fig. 9. Estimated disturbance $\hat{\boldsymbol{\epsilon}}$ in the $\alpha\beta$ reference frame under the parameter mismatch of $r_{L_m} = 67\%$, as shown in Figs. 7 and 8 for (a) one-step ($N_p = 1$) and (b) five-step ($N_p = 5$) FCS-MPC. (a) $N_p = 1$. (b) $N_p = 5$.

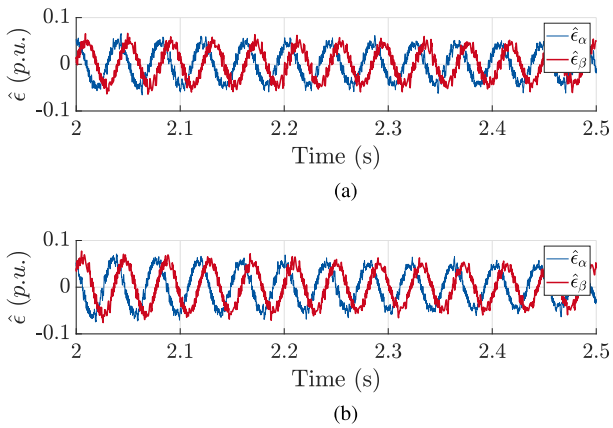

Fig. 10. Estimated disturbance $\hat{\boldsymbol{\epsilon}}$ in the $\alpha\beta$ reference frame under the parameter mismatch of $r_{L_m} = 150\%$, as shown in Figs. 7 and 8 for (a) one-step ($N_p = 1$) and (b) five-step ($N_p = 5$) FCS-MPC. (a) $N_p = 1$. (b) $N_p = 5$.

with $N_p = 1$ and $N_p = 5$ are shown in Figs. 9 and 10, respectively.

C. Comparison of the Total Demand Distortion (TDD)

The TDD is an essential indicator for evaluating the performance of multistep FCS-MPC. Therefore, the TDD from the previous tests is investigated. Moreover, since the proposed method has different switching frequencies from the conventional multistep FCS-MPC during the aforementioned tests, the TDD of the conventional multistep FCS-MPC with a comparable switching frequency is also assessed. The corresponding TDD is computed by means of

$$\text{TDD} = \frac{1}{\sqrt{2}\, I_N} \sqrt{\sum_{j \neq 1} i_{s,j}^2}. \tag{21}$$

The TDD values from various test cases are computed and summarized in Fig. 11. The parameter variation has influence on the solution of the control problem and can further affect

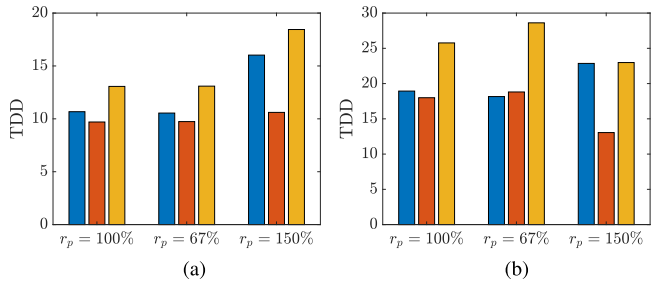

Fig. 11. Comparison of TDDs at the steady state of the IM. The TDD of the conventional FCS-MPC with the switching frequency, as shown in Figs. 7 ($N_p = 1$) and 8 ($N_p = 5$), is shown in blue. The TDD of the proposed method is denoted in red. The TDD of the conventional FCS-MPC at a similar switching frequency to the proposed method is given in yellow. (a) $N_p = 1$. (b) $N_p = 5$.

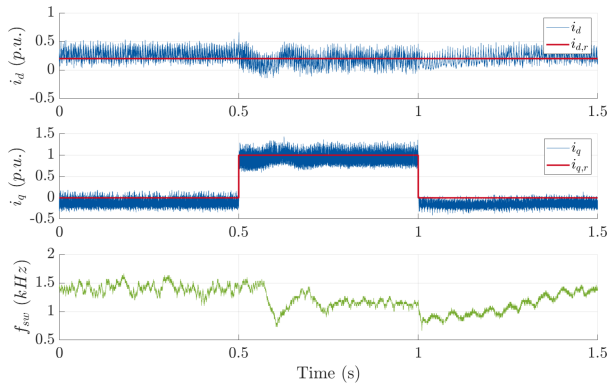

Fig. 12. Performance of the conventional FCS-MPC with $N_p = 5$ during transient of the load step.

the switching frequency. Therefore, the TDD of multistep FCS-MPC with a similar switching frequency to the proposed method is investigated for the purpose of a fair comparison and shown in Fig. 11. It can be concluded that the proposed method has lower TDDs than the conventional multistep FCS-MPC with a similar or even a much higher switching frequency.

D. Performance Under the Load Step

The transient performance of the proposed control strategy is tested under a load step from the no-load condition to the full-load condition, which is given at $t = 0.5\,\text{s}$ and a load step back to the no-load condition at $t = 1\,\text{s}$.

A steady-state error can be observed in Fig. 12 from $t = 0\,\text{s}$ to $t = 0.5\,\text{s}$, where the conventional multistep FCS-MPC is applied. It can be explained by the fact that the parameters in Table I can be different from the real motor parameters and the compensation of the digital delay may be inaccurate. After the first load step, the conventional multistep FCS-MPC reaches the new steady state after around $0.25\,\text{s}$. Moreover, a small offset can be noticed at the new steady state. After the second step, the currents still converge slowly toward their desired values, while a noticeable steady-state error still exists. In comparison to the previous results with the conventional multistep FCS-MPC, the proposed method shows more accurate tracking results and converges to the desired reference value immediately after the

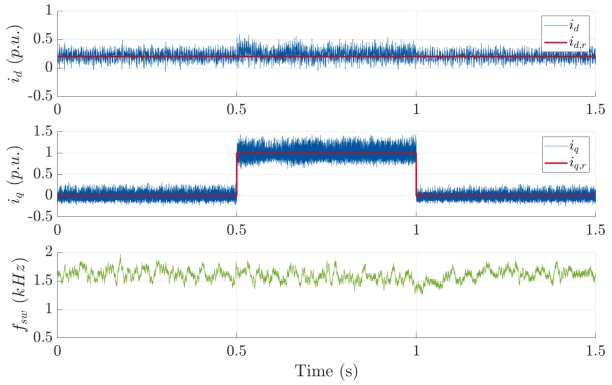

Fig. 13. Performance of the proposed method with $N_p = 5$ during transient of the load step.

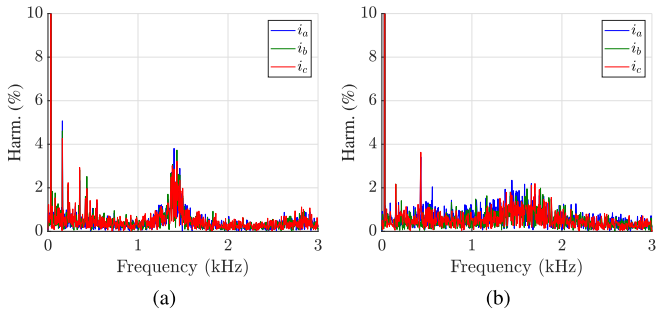

Fig. 14. Stator current harmonic spectra for (a) conventional FCS-MPC and (b) proposed method.

steps. Especially after the step $t = 1\,\mathrm{s}$, the proposed method outperforms the conventional multistep FCS-MPC regarding the tracking ability during both steady state and transients. More specifically, obvious steady-state errors can be observed with conventional multistep FCS-MPC, i.e., around 30% of i_d and up to 25% on the q-coordinate of the full-load current. In contrast to that, the proposed method eliminates the steady-state errors. It is worth mentioning that the switching frequency remains relatively constant when the proposed method is utilized, which could be explained by the fact that, thanks to the inclusion of the estimated disturbance term $\hat{\epsilon}$, the motor parameter variation caused by the torque step is fully compensated for.

For a deeper insight into the proposed method, the current harmonic spectra from the steady-state operating point in Figs. 12 and 13 from $t = 0.5\,\mathrm{s}$ to $t = 1\,\mathrm{s}$, i.e., $i_d = 0.2\,\mathrm{p.u.}$ and $i_q = 1\,\mathrm{p.u.}$, are shown in Fig. 14. The harmonic content is computed in the per unit system. In both harmonic spectra, significant harmonic energy around the switching frequency can be noticed. However, the proposed method has smaller harmonic content around the switching frequency. Compared with the conventional multistep FCS-MPC, it can be observed that the harmonic energy of the proposed method is lower, as also quantified by the TDD, which is around 17%, as opposed to the TDD of the conventional multistep FCS-MPC, which is more than 25%. Moreover, as can be seen in Fig. 14, the harmonic

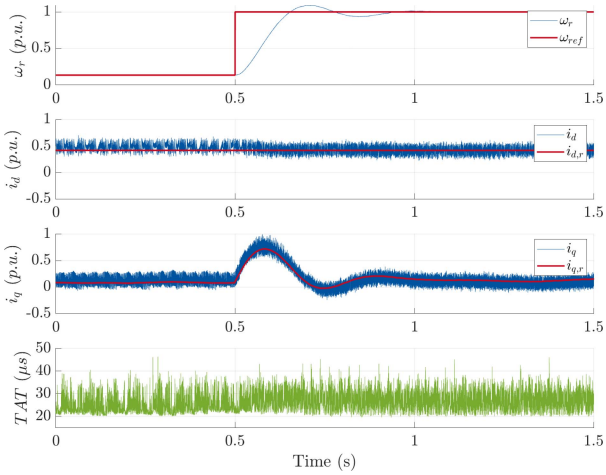

Fig. 15. Performance of the conventional FCS-MPC with $N_p = 5$ under a step-up change in the speed reference.

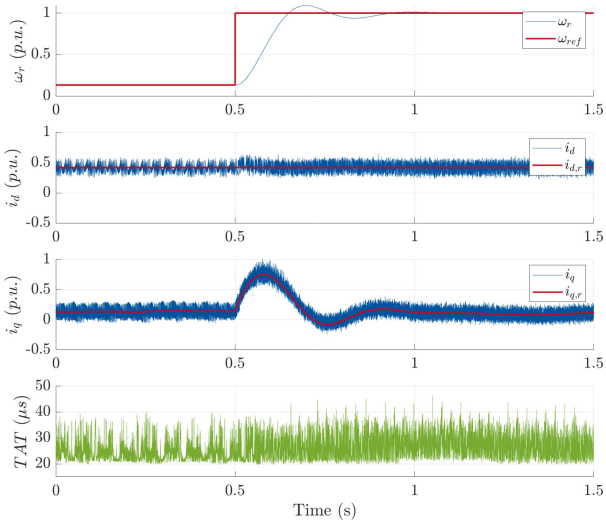

Fig. 16. Performance of the proposed method with $N_p = 5$ under a step-up change in the speed reference.

energy at low frequencies is lower, implying that it could be easier filtered out, if needed.

E. Performance Under the Speed Step

The transient behavior of the proposed method is further tested under a speed step from 300 r/min to the rated speed. The speed step was given at $t = 0.5\,\mathrm{s}$. The turnaround times of the conventional multistep FCS-MPC and the proposed method are recorded and denoted in the figures as TAT. The corresponding results are shown in Figs. 15 and 16.

It can be observed from Figs. 15 and 16 that the proposed method improved the tracking accuracy in a wide range of speed values, both on the d- and q-axis. Thanks to the inclusion of the disturbance state in the system model, the DOB can effectively address the mismatch caused by the wrong speed applied in the prediction model and avoid any steady-state error. Even though comparing with the conventional multistep FCS-MPC,

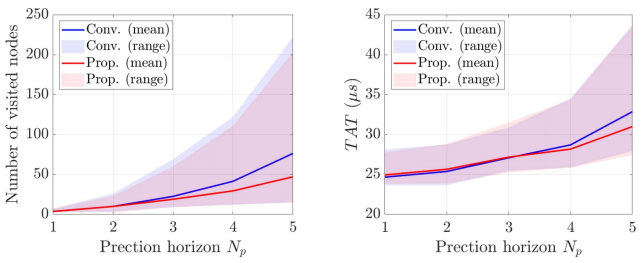

Fig. 17. Computational burden of the conventional FCS-MPC and the proposed method in relationship with the prediction horizon N_p. (a) Represents the number of visited nodes by the sphere decoding algorithm. (b) Shows the turnaround time (TAT) of the respective control algorithms.

the proposed method has an additional disturbance observing mechanism, the execution time, which is evaluated by the turnaround time, does not apparently increase. On the contrary, the turnaround time is reduced at the low-speed operation (before $t = 0.5\,\mathrm{s}$).

F. Evaluation of the Computational Burden

In order to better demonstrate and compare the computational burden of both methods, the number of visited nodes by the sphere decoding algorithm and the turnaround time are evaluated regarding various prediction horizons. The experimental results are shown in Fig. 17. As can be seen in that figure, the proposed method has comparable computational complexity with that of the conventional multistep FCS-MPC. Moreover, it is worth noting that the average computational cost of the proposed algorithm is smaller than that of the conventional multistep FCS-MPC, a difference that becomes more evident as the length of the horizon increases.

V. Conclusion

In this article, an observer-augmented multistep FCS-MPC control strategy is proposed, which improves the controller robustness against disturbances for an IM-drive system, including external disturbances, parameter mismatches, and model uncertainties. As it is shown in the simulations, the parameter mismatch problem will not necessarily affect the solution of the conventional multistep FCS-MPC. But its influence is not negligible. Besides, because the optimization problem is built on the system dynamics of the nominal system, the error caused by the disturbances accumulates with the increase of the prediction horizon. The proposed method estimates the disturbances resulted from the parameter mismatches and the unmodeled uncertainties with a DOB. The estimation results, including the system states and the disturbances, are delivered to the controller to compute the switching sequence. As a result, the flux observer of the conventional multistep FCS-MPC for the current control in IM is omitted.

The proposed method is compared with the conventional multistep FCS-MPC at the steady state and outperforms it in terms of tracking accuracy and the TDD of the current. Moreover, the proposed method is tested under the load step and shows a better transient performance. It also shows better tracking accuracy under the speed-step test. After the analysis of the harmonic spectra, it can be concluded that the proposed method has different harmonic distribution from the conventional method. More specifically, it has a smaller harmonic content around the switching frequency and at low frequencies. The execution time of the proposed time is also evaluated with the turnaround time and the visited nodes as metrics. As shown, the computational burden of the proposed control strategy is similar to that of the conventional multistep FCS-MPC in terms of the worst-case scenario, and less on average, especially as the horizon increases.

References

[1] S. Vazquez, J. Rodríguez, M. Rivera, L. G. Franquelo, and M. Norambuena, "Model predictive control for power converters and drives: Advances and trends," *IEEE Trans. Ind. Electron.*, vol. 64, no. 2, pp. 935–947, Feb. 2017.
[2] J. Lee, "Model predictive control: Review of the three decades of development," *Int. J. Control, Autom. Syst.*, vol. 9, pp. 415–424, 2011.
[3] M. Morari and J. H. Lee, "Model predictive control: Past, present and future," *Comput. Chem. Eng.*, vol. 23, no. 4, pp. 667–682, 1999. [Online]. Available: http://www.sciencedirect.com/science/article/pii/S0098135498003019
[4] J. Scoltock, T. Geyer, and U. K. Madawala, "A comparison of model predictive control schemes for MV induction motor drives," *IEEE Trans. Ind. Inform.*, vol. 9, no. 2, pp. 909–919, May 2013.
[5] H. Miranda, P. Cortes, J. I. Yuz, and J. Rodríguez, "Predictive torque control of induction machines based on state-space models," *IEEE Trans. Ind. Electron.*, vol. 56, no. 6, pp. 1916–1924, Jun. 2009.
[6] E. Fuentes, D. Kalise, J. Rodríguez, and R. M. Kennel, "Cascade-free predictive speed control for electrical drives," *IEEE Trans. Ind. Electron.*, vol. 61, no. 5, pp. 2176–2184, May 2014.
[7] J. Rodríguez et al., "State of the art of finite control set model predictive control in power electronics," *IEEE Trans. Ind. Inform.*, vol. 9, no. 2, pp. 1003–1016, May 2013.
[8] T. Geyer and D. E. Quevedo, "Performance of multistep finite control set model predictive control for power electronics," *IEEE Trans. Power Electron.*, vol. 30, no. 3, pp. 1633–1644, Mar. 2015.
[9] P. Cortés, A. Wilson, S. Kouro, J. Rodríguez, and H. Abu-Rub, "Model predictive control of multilevel cascaded H-bridge inverters," *IEEE Trans. Ind. Electron.*, vol. 57, no. 8, pp. 2691–2699, Aug. 2010.
[10] M. Vatani, B. Bahrani, M. Saeedifard, and M. Hovd, "Indirect finite control set model predictive control of modular multilevel converters," *IEEE Trans. Smart Grid*, vol. 6, no. 3, pp. 1520–1529, May 2015.
[11] W. Tian, X. Gao, and R. Kennel, "Model predictive control of modular multilevel converters with independent arm-balancing control," in *Proc. IEEE Int. Symp. Predictive Control Elect. Drives Power Electron.*, 2019, pp. 1–5.
[12] W. Xie et al., "Finite-control-set model predictive torque control with a deadbeat solution for PMSM drives," *IEEE Trans. Ind. Electron.*, vol. 62, no. 9, pp. 5402–5410, Sep. 2015.
[13] M. Habibullah, D. D. Lu, D. Xiao, and M. F. Rahman, "A simplified finite-state predictive direct torque control for induction motor drive," *IEEE Trans. Ind. Electron.*, vol. 63, no. 6, pp. 3964–3975, Jun. 2016.
[14] T. Geyer, P. Karamanakos, and R. Kennel, "On the benefit of long-horizon direct model predictive control for drives with LC filters," in *Proc. IEEE Energy Convers. Congr. Expo.*, 2014, pp. 3520–3527.
[15] I. Alevras, P. Karamanakos, S. Manias, and R. Kennel, "Variable switching point predictive torque control with extended prediction horizon," in *Proc. IEEE Int. Conf. Ind. Technol.*, 2015, pp. 2352–2357.
[16] T. Geyer and D. E. Quevedo, "Multistep finite control set model predictive control for power electronics," *IEEE Trans. Power Electron.*, vol. 29, no. 12, pp. 6836–6846, Dec. 2014.
[17] P. Karamanakos and T. Geyer, "Guidelines for the design of finite control set model predictive controllers," *IEEE Trans. Power Electron.*, vol. 35, no. 7, pp. 7434–7450, Jul. 2020.
[18] T. Dorfling, H. du Toit Mouton, T. Geyer, and P. Karamanakos, "Long-horizon finite-control-set model predictive control with nonrecursive sphere decoding on an FPGA," *IEEE Trans. Power Electron.*, vol. 35, no. 7, pp. 7520–7531, Jul. 2020.

[19] P. Acuna, C. A. Rojas, R. Baidya, R. P. Aguilera, and J. E. Fletcher, "On the impact of transients on multistep model predictive control for medium-voltage drives," *IEEE Trans. Power Electron.*, vol. 34, no. 9, pp. 8342–8355, Sep. 2019.
[20] R. Baidya et al., "Enabling multistep model predictive control for transient operation of power converters," *IEEE Open J. Ind. Electron. Soc.*, vol. 1, pp. 284–297, 2020, doi: 10.1109/OJIES.2020.3029358.
[21] P. Karamanakos, T. Geyer, and R. P. Aguilera, "Long-horizon direct model predictive control: Modified sphere decoding for transient operation," *IEEE Trans. Ind. Appl.*, vol. 54, no. 6, pp. 6060–6070, Nov./Dec. 2018.
[22] H. A. Young, M. A. Perez, and J. Rodríguez, "Analysis of finite-control-set model predictive current control with model parameter mismatch in a three-phase inverter," *IEEE Trans. Ind. Electron.*, vol. 63, no. 5, pp. 3100–3107, May 2016.
[23] O. I. Okoro, "Dynamic and thermal mode model of induction machine with non-linear effects," Ph.D. dissertation, Elect. Eng., Universität Kassel, Kassel, Germany, 2002.
[24] A. Bemporad and M. Morari, "Robust model predictive control: A survey," in *Robustness in Identification and Control*, A. Garulli and A. Tesi, Eds. London, U.K.: Springer, 1999, pp. 207–226.
[25] M. Preindl, "Robust control invariant sets and Lyapunov-based MPC for IPM synchronous motor drives," *IEEE Trans. Ind. Electron.*, vol. 63, no. 6, pp. 3925–3933, Jun. 2016.
[26] R. P. Aguilera, P. Lezana, and D. E. Quevedo, "Finite-control-set model predictive control with improved steady-state performance," *IEEE Trans. Ind. Inform.*, vol. 9, no. 2, pp. 658–667, May 2013.
[27] C.-K. Lin, J.-T. Yu, Y.-S. Lai, and H.-C. Yu, "Improved model-free predictive current control for synchronous reluctance motor drives," *IEEE Trans. Ind. Electron.*, vol. 63, no. 6, pp. 3942–3953, Jun. 2016.
[28] F. Tinazzi, P. G. Carlet, S. Bolognani, and M. Zigliotto, "Motor parameter-free predictive current control of synchronous motors by recursive least-square self-commissioning model," *IEEE Trans. Ind. Electron.*, vol. 67, no. 11, pp. 9093–9100, Nov. 2020.
[29] S. Kwak, U. Moon, and J. Park, "Predictive-control-based direct power control with an adaptive parameter identification technique for improved AFE performance," *IEEE Trans. Power Electron.*, vol. 29, no. 11, pp. 6178–6187, Nov. 2014.
[30] Y. Xu, N. Parspour, and U. Vollmer, "Torque ripple minimization using online estimation of the stator resistances with consideration of magnetic saturation," *IEEE Trans. Ind. Electron.*, vol. 61, no. 9, pp. 5105–5114, Sep. 2014.
[31] O. Wallscheid and E. F. B. Ngoumtsa, "Investigation of disturbance observers for model predictive current control in electric drives," *IEEE Trans. Power Electron.*, vol. 35, no. 12, pp. 13563–13572, Dec. 2020.
[32] J. Wang, F. Wang, Z. Zhang, S. Li, and J. Rodríguez, "Design and implementation of disturbance compensation-based enhanced robust finite control set predictive torque control for induction motor systems," *IEEE Trans. Ind. Inform.*, vol. 13, no. 5, pp. 2645–2656, Oct. 2017.
[33] L. Yan, M. Dou, Z. Hua, H. Zhang, and J. Yang, "Robustness improvement of FCS-MPTC for induction machine drives using disturbance feedforward compensation technique," *IEEE Trans. Power Electron.*, vol. 34, no. 3, pp. 2874–2886, Mar. 2019.
[34] M. S. Mousavi, S. A. Davari, V. Nekoukar, C. Garcia, and J. Rodríguez, "A robust torque and flux prediction model by a modified disturbance rejection method for finite-set model-predictive control of induction motor," *IEEE Trans. Power Electron.*, vol. 36, no. 8, pp. 9322–9333, Aug. 2021.
[35] C. Xu, Z. Han, and S. Lu, "Deadbeat predictive current control for permanent magnet synchronous machines with closed-form error compensation," *IEEE Trans. Power Electron.*, vol. 35, no. 5, pp. 5018–5030, May 2020.
[36] T. Geyer and D. E. Quevedo, "Multistep direct model predictive control for power electronics—Part 1: Algorithm," in *Proc. IEEE Energy Convers. Congr. Expo.*, 2013, pp. 1154–1161.
[37] X. Li and R. Kennel, "Comparison of state-of-the-art estimators for electrical parameter identification of PMSM," in *Proc. IEEE Int. Symp. Predictive Control Elect. Drives Power Electron.*, 2019, pp. 1–6.
[38] R. P. Aguilera and D. E. Quevedo, "Predictive control of power converters: Designs with guaranteed performance," *IEEE Trans. Ind. Inform.*, vol. 11, no. 1, pp. 53–63, Feb. 2015.
[39] P. Karamanakos, T. Geyer, and R. Kennel, "On the choice of norm in finite control set model predictive control," *IEEE Trans. Power Electron.*, vol. 33, no. 8, pp. 7105–7117, Aug. 2018.
[40] F. Alonge, T. Cangemi, F. D'Ippolito, A. Fagiolini, and A. Sferlazza, "Convergence analysis of extended Kalman filter for sensorless control of induction motor," *IEEE Trans. Ind. Electron.*, vol. 62, no. 4, pp. 2341–2352, Apr. 2015.
[41] R. Schneider and C. Georgakis, "How to not make the extended Kalman filter fail," *Ind. Eng. Chem. Res.*, vol. 52, pp. 3354–3362, 2013.

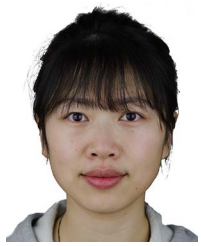

Xinyue Li was born in Yunnan, China, in 1991. She received the B.S. degree in electrical engineering from Tsinghua University, Beijing, China, in 2013, the M.S. degree in electrical engineering, information technology, and computer engineering from RWTH Aachen University, Aachen, Germany, in 2017, and the Dr.-Ing. (Ph.D.) degree from the Technical University of Munich, Munich, Germany, in 2022.

From 2017 to 2022, she was with Bosch Group and took several positions in different business units. Since 2023, she has been with Mercedes-Benz AG, Stuttgart, Germany. Her research interests include control of power electronics, parameter identification, and robust and optimal control of ac machines.

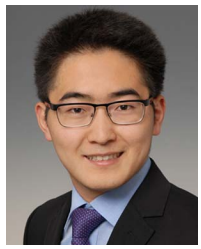

Wei Tian (Member, IEEE) received the B.Eng. degree in electrical engineering and automation from Central South University, Changsha, China, in 2012, and the M.Sc. degree in electrical power engineering from RWTH Aachen University, Aachen, Germany, in 2015. He is currently working toward the Ph.D. degree with the Technical University of Munich (TUM), Munich, Germany.

He is the Chair of Electrical Drive Systems and Power Electronics and High-Power Converter Systems with TUM, Munich, Germany. His research interests include power electronics and electrical drives, model predictive control, and modular multilevel converter.

Qifan Yang (Graduate Student Member, IEEE) was born in Anqing, China, in 1995. He received the B.Eng. degree in electrical engineering from Xi'an Jiaotong University, Xi'an, China, in 2016, and the M.Sc. degree in electrical power engineering in 2019 from the Technical University of Munich, Munich, Germany, where he is currently working toward the Ph.D. degree.

He is the Chair of Electrical Drive Systems and Power Electronics with TUM, Munich, Germany. His research interests include optimal control, power electronics, and electrical drives.

Petros Karamanakos (Senior Member, IEEE) received the Diploma and Ph.D. degrees in electrical and computer engineering from the National Technical University of Athens, Athens, Greece, in 2007 and 2013, respectively.

From 2010 to 2011, he was with ABB Corporate Research Center, Baden-Dättwil, Switzerland, where he worked on model predictive control strategies for medium-voltage drives. From 2013 to 2016, he was a Postdoctoral Research Associate with the Chair of Electrical Drive Systems and Power Electronics, Technische Universität München, Munich, Germany. Since 2016, he has been with the Faculty of Information Technology and Communication Sciences, Tampere University, Tampere, Finland, where he is currently an Associate Professor. His main research interests lie at the intersection of optimal control, mathematical programming, and power electronics, including model predictive control and optimal modulation for utility-scale power converters and ac variable speed drives.

Dr. Karamanakos was a recipient of the 2014 Third Best Paper Award of the IEEE Transactions on Industry Applications and three Prize Paper Awards at conferences. He serves as an Associate Editor for the IEEE TRANSACTIONS ON INDUSTRY APPLICATIONS. He is a Regional Distinguished Lecturer of the IEEE Power Electronics Society in the years 2022 and 2023.

Ralph Kennel (Life Fellow, IEEE) was born in Kaiserslautern, Germany, in 1955. He received the Diploma and Dr.-Ing. (Ph.D.) degrees from the University of Kaiserslautern, Kaiserslautern, Germany, in 1979 and 1984, respectively.

From 1983 to 1999, he was with Robert BOSCH GmbH, Germany, working on several positions. Until 1997, he was responsible for the development of servo drives. From 1994 to 1999, he was a Visiting Professor with the University of Newcastle-upon-Tyne, Newcastle-upon-Tyne, U.K. From 1999 to 2008, he was a Professor of electrical machines and drives with Wuppertal University, Wuppertal, Germany. Since 2008, he has been a Professor of electrical drive systems and power electronics with the Technical University of Munich, Munich, Germany. His current main research interests include sensorless control of ac drives, predictive control of power electronics, and hardware-in-the-loop systems.

Dr. Kennel is a Fellow of IET (former IEE) and a Chartered Engineer in the U.K. Within IEEE, he was Treasurer of the Germany Section as well as ECCE Global Partnership Chair of the Power Electronics Society. He is an Associate Editor for the IEEE TRANSACTIONS ON POWER ELECTRONICS.